Computers in Biology and Medicine 136 (2021) 104652

Contents lists available at ScienceDirect

Computers in Biology and Medicine

journal homepage: www.elsevier.com/locate/compbiomed

Efficient parallel simulation of hemodynamics in patient-specific abdominal aorta with aneurysm

Shanlin Qin [a], Bokai Wu [a], Jia Liu [a], Wen-Shin Shiu [a], Zhengzheng Yan [a], Rongliang Chen [a,b,*], Xiao-Chuan Cai [c,**]

[a] Shenzhen Institutes of Advanced Technology, Chinese Academy of Sciences, Shenzhen, China
[b] Shenzhen Key Laboratory for Exascale Engineering and Scientific Computing, Shenzhen, China
[c] Department of Mathematics, University of Macau, Macau, China

ARTICLE INFO

Keywords:
Blood flow
Abdominal aorta with aneurysm
Finite element
Fully implicit time integration
Domain decomposition
Parallel computing

ABSTRACT

Surgical planning for aortic aneurysm repair is a difficult task. In addition to the morphological features obtained from medical imaging, alternative features obtained with computational modeling may provide additional useful information. Though numerical studies are noninvasive, they are often time-consuming, especially when we need to study and compare multiple repair scenarios, because of the high computational complexity. In this paper, we present a highly parallel algorithm for the numerical simulation of unsteady blood flows in the patient-specific abdominal aorta before and after the aneurysmic repair. We model the blood flow with the unsteady incompressible Navier-Stokes equations with different outlet boundary conditions, and solve the discretized system with a highly scalable domain decomposition method. With this approach, a high resolution simulation of a full-size adult aorta can be obtained in less than an hour, instead of days with older methods and software. In addition, we show that the parallel efficiency of the proposed method is near 70% on a parallel computer with 2,880 processor cores.

1. Introduction

The abdominal aneurysm is an abnormal bulge or diffused expansion of a portion of the abdominal aorta. Surgical intervention is often required for the treatment of the aneurysm by introducing a reshaping of the aneurysmal region. An accurate pre- and post-operative rupture risk assessment of the abdominal aortic aneurysm has significant guiding importance for the surgical plannning of an aortic aneurysm repair surgery. Clinical studies correlate the risk to the maximum aneurysmatic diameter based on medical imaging technologies [23,36]. However, it is widely believed that the risk is not necessarily reflected by the maximum diameter alone [16,42]. Therefore, additional information is necessary for the accurate risk assessment of an aneurysm before and after the surgical repair.

Biomechanical indices [40], hemodynamic factors [8], geometrical features [21,32] and pathological factors [19] have been suggested as promising predictive quantities for diagnosing and managing the aortic aneurysmal diseases. To obtain these quantities, various computational methods have been used, such as model order reduction [9], machine learning [20] and Bayesian inference [1]. This work focuses on the computational fluid dynamics (CFD), which involves a compuational analysis of the blood flow by combining a computational method with medical imaging, such as the computed tomography. This image-based computation enables a quantitative description of the blood flow by solving the Navier-Stokes equations. Not only can it noninvasively provide, for example, the blood pressure and pulse wave velocity on surgically inaccessible blood vessels, but also derive the directly immeasurable quantities, such as the wall shear stress (WSS) [35]. Earlier numerical studies were restricted to hypothetical aortic geometries, including simple axisymmetric [13] and asymmetrical [14] structures. More recently, realistic simulations often adopt the patient-specific geometries, most of which can be categorized into two major classes: the pure fluid modeling known as CFD and the fluid flow modeling coupled with a viscoelastic vessel wall known as the fluid-structure interaction. We focus on CFD problems in this paper and below we provide a brief review of the state of the art approaches for the

* Corresponding author. Shenzhen Key Laboratory for Exascale Engineering and Scientific Computing, Shenzhen, China.
** Corresponding author.
E-mail addresses: rl.chen@siat.ac.cn (R. Chen), xccai@um.edu.mo (X.-C. Cai).

https://doi.org/10.1016/j.compbiomed.2021.104652
Received 17 May 2021; Received in revised form 30 June 2021; Accepted 13 July 2021
Available online 24 July 2021

Table 1
List of references with simulation details.

Publications	Geometric models	Number of elements	Outlet boundary conditions	Solution algorithms (software package)	Number of processor cores	Computing time
Kumar et al., 2017 [27]	9-outlet full-size normal aorta	1.38 million tetrahedral elements	Opening boundary condition (static pressure 120 mmHg)	Finite volume method (ANSYS-CFX)	– –	– –
Vinoth et al., 2019 [50]	9-outlet full-size normal & aneurysmal aortas	1.49 million tetrahedral elements	Opening boundary condition (static pressure 120 mmHg)	Finite volume method (ANSYS-CFX)	– –	– –
Antón et al., 2015 [2]	2-outlet abdominal aortic aneurysm	1.40 million tetrahedral elements	Given flow split ratio	Finite volume method (ANSYS-FLUENT)	– –	– –
Vergara et al., 2017 [48]	2-outlet abdominal aortic aneurysm	0.28 million tetrahedral elements	Zero stress	SUPG stabilized P2–P2 finite element method (LifeV)	– –	– –
Arzani 2018 [3]	2-outlet cerebral artery & abdominal aorta with aneurysms	3.53 & 4.70 million tetrahedral elements	Zero traction & resistance boundary conditions)	P_1–P_1 finite element method (Oasis)	– –	– –
Polanczyk & Piechota 2010 [39]	2-outlet real & virtual abdominal aorta with aneurysm	0.60 & 0.9 million tetrahedral elements	Given flow rate	Finite volume method (ANSYS-CFX)	– –	25 h
Hardman et al., 2013 [18]	2-outlet abdominal aortic aneurysm	2.16 million tetrahedral elements	– –	Finite volume method (ANSYS-FLUENT)	– –	6 days
Owen et al., 2016 [37]	2-outlet abdominal aortic aneurysm	1.7 million polyhedral elements	– –	Finite volume method (STAR CCM +)	64	45 min
Les et al., 2010 [30]	10-outlet abdominal aorta with aneurysm (8 patients)	9.05 million tetrahedral elements	Three–element Windkessel	Stabilized finite element method (SimVascular)	96	3–7 days
Updegrove et al., 2017 [47]	Pulmonary arteries & full-size aorta & coronary artery	No specific number of tetrahedral elements	Resistance & three–element Windkessel & lumped parameter network	SUPG & PSPG stabilized P1–P1 finite element method (SimVascular)	– –	– –
Zhou et al., 2010 [56]	Several–outlet abdominal aortic aneurysm	1.07 billion tetrahedral elements	Three–element Windkessel	Stabilized finite element method (PHASTA)	163840	– –
Groen et al., 2013 [17]	Intracranial vasculature	44.65 million fluid lattice sites	Given velocity or pressure	Lattice Boltzmann method	32768	About 0.1s for 100 time stpes
Auricchio et al., 2018 [4]	3-outlet thoracic aorta	6.70 million tetrahedral elements	Three–element Windkessel	Bubble stabilized finite element method (LifeV)	2048	– –

modeling of blood flows in the abdominal aorta.

Different numerical methods have been proposed for accurately simulating of blood flows in the abdominal aorta. Kumar et al. studied the steady and transient blood flows by using ANSYS CFX and reported that the detailed branches have significant impact on the resulting flow patterns [27,50]. Antón et al. applied a second-order implicit finite volume scheme implemented on the commercial package FLUENT to analyze the aortic pressure field [2]. More recently, Vergara et al. considered a large eddy simulation to study the turbulent effects of blood flows, in which a semi-implicit approach and a SUPG stabilized P_2–P_2 finite element method were used for the temporal and spatial discretizations, respectively [48]. Arzani used an open source P_2–P_1 finite element software to simulate blood flows in the cerebral artery and the abdominal aorta with aneurysms [3].

For the computational approach to be clinically useful in the surgical planning, the overall computational time has to be short to allow comparisons among multiple surgery choices. Les et al. used a stabilized finite element method to model the blood flow in the aneurysmal aorta [30]. The calculation took approximately 3–7 days using 96 cores for meshes with several million elements and a week using 200 cores for a mesh with 31.8 millon elements. Polanczyk and Piechota reported that it took them 25 h to simulate the blood flow in the abdominal aorta using FLUENT on a mesh with around 600, 000 elements [39]. Using the same software, Hardman et al. spent 6 days to obtain the CFD simulation on meshes with about 2 millions elements for 200 time steps [18]. By running a commercial parallel finite volume solver on 64 cores, Owen et al. took 45 min to simulate the blood flow in a small portion of the abdominal aorta, where the number of elements is about 1.7 million and the number of time steps is 5500 [37].

To reduce the computing time and increase the numerical accuracy in the modeling of blood flows, most of the latest developments target supercomputers with a large number of processor cores [15,33,55]. There are several open-source software packages that support parallel computing for patient-specific blood flow simulations. The widely used

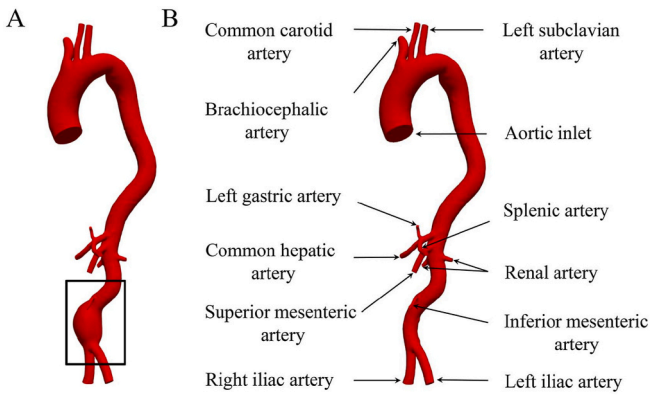

Fig. 1. (A) pre-operative aorta with an abdominal aneurysm and (B) post-operative aorta with the aneurysm removed. An inlet and 12 outlet branches are labeled.

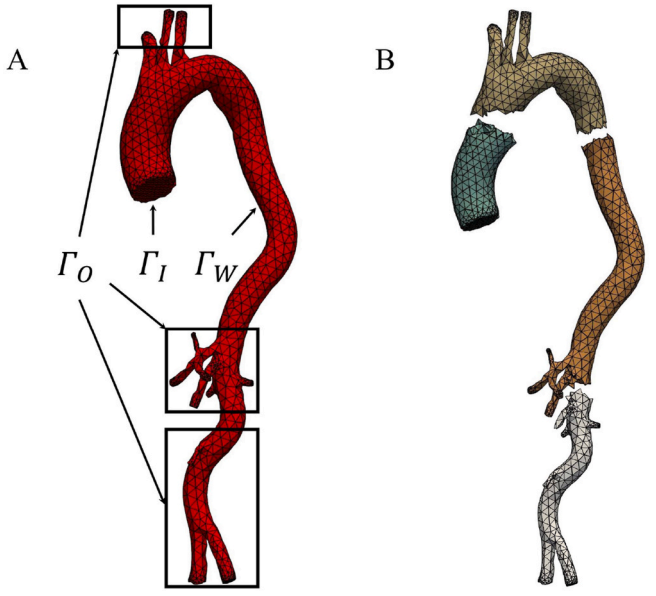

Fig. 2. (A) A sample mesh for the post-operative aorta and (B) a partition of the global mesh into four subdomains for parallel processing.

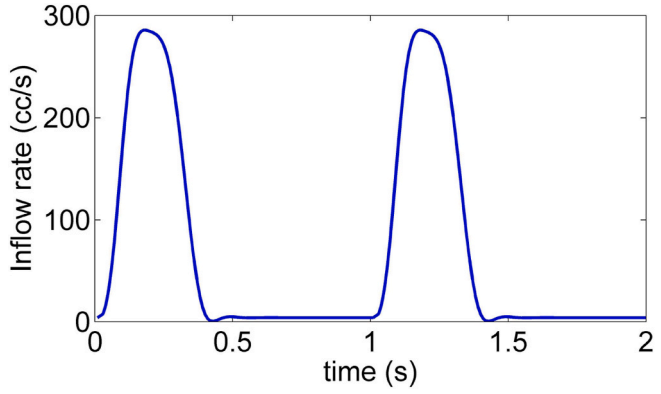

Fig. 3. The pulsatile inflow rate profile for two cardiac cycles.

SimVascular [28] and CRIMSON [24] provide a complete pipeline from the image segmentation to the blood flow simulation and analysis [24,30,47]. The software has a nice and easy-to-use interface. Its algebraic solver is built on PHASTA [55,56], which is based on a Newton-Krylov method and has a major drawback as it doesn't have any preconditioners. As a result, its linear and nonlinear solvers can only handle relatively well-conditioned problems or problems with small time steps [49]. In the present paper, with a rather powerful overlapping domain decomposition preconditioner, our linear and nonlinear solvers are more robust and allow large time steps.

HemeLB [33] is based on the lattice-Boltzmann method (LBM) and it scales well to 32768 cores for simulations of intracranial aneurysm hemodynamics with approximately 45 million lattices. LBM is easy to implement on Cartesian grid but rather difficult to implement for complex boundary conditions defined on irregular boundaries [17,31]. LifeV [7] is a finite element library that provides a platform for developing and testing numerical methods. In a recent work, it was used to solve a hemodynamical problem of 3-outlet thoracic aorta and shown to scale with up to 2048 cores for a problem discretized on a mesh with 6.70 million tetrahedral elements [4]. In Table 1, we provide a quick summary of the recent publications including methods used and computational capabilities for hemodynamic problems.

In this paper, we study a highly parallel algorithm to solve the unsteady incompressible Navier-Stokes equations with different outlet boundary conditions. Comparing with the traction-free outlet boundary condition, the resistance outlet boundary condition assumes a linear dependence between the pressure and the flow rate at each outlet through the integral of the velocity. Although the integral-type boundary condition is more accurate to represent the downstream arterial networks, it is computationally nontrivial due to the existence of the integral, which increases the communication burden between processor cores and therefore degrades the parallel performance of the numerical solver. The correctness of the proposed numerical method and the mesh-independence of the numerical solution are studied before its application to the blood flow simulation in a full-size adult aneurysmal aorta before and after the repair. The proposed approach greatly reduces the simulation time so that multiple operation choices can be studied and compared during the surgical planning. Clinical investigation of the proposed methods is out of the scope of this paper.

The rest of this paper is organized as follows. In Section 2, abdominal aortas and their mesh partition are introduced; then the governing equations and numerical methods are presented, including the implicit finite element discretization and the Newton-Krylov-Schwarz method. In Section 3, we study the influence of different outlet boundary conditions and the blood flow of two patient-specific cases acquired before and after the aneurysm repair, and analyze the parallel scalability of the algorithm. In Section 4, we draw some conclusions.

2. Problem description and solution methods

2.1. Image segmentation and mesh partition

As shown in Fig. 1, a CFD-supported surgical planning is studied in the pre-operative aorta with an abdominal aneurysm and the post-operative aorta with the aneurysm removed. Both geometries, denoted as $\Omega \in \mathbb{R}^3$, have one inlet and 12 outlets. Taking the post-operative aorta as an example in Fig. 2, we label the inlet as Γ_I, the wall as Γ_W, and the outlets as Γ_{O_i} ($i = 1, 2 \ldots, m$ with m being the total number of outlets) for the prescription of different boundary conditions. An unstructured mesh Ω_h consisting of tetrahedral elements is generated to cover the computational domain Ω and a schematic representation of a 3D coarse aortic mesh is shown in Fig. 2 A. To run the simulation on a parallel computer, the mesh is partitioned into N non-overlapping submeshes by ParMETIS [22], denoted as Ω_h^l ($l = 1, \ldots, N$), where N is the total number of processor cores. The ParMETIS ensures roughly the same number of elements in each subregion to achieve load balance. All vectors and matrices associated with a subdomain are mapped to the same processor core of the parallel computer. A sample partition with 4 sub-meshes highlighted using different colors is presented in Fig. 2 B. A detailed

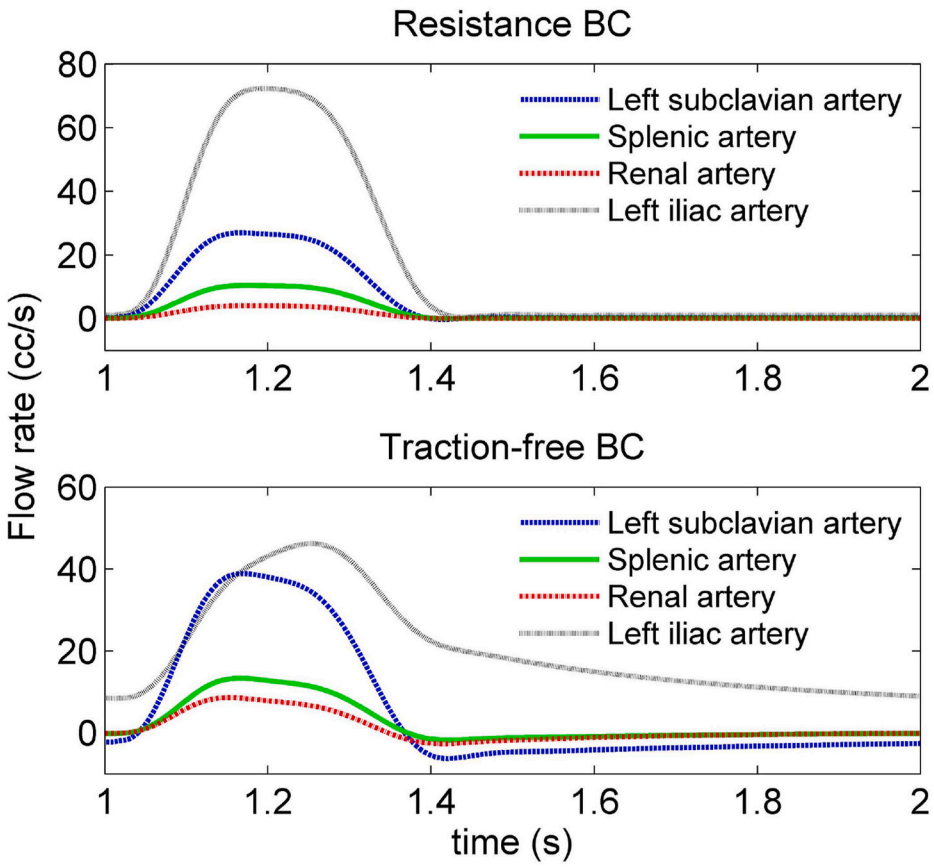

Fig. 4. The plots of outflow rates from the resistance and traction-free boundary conditions for four branches: the left subclavian artery, the splenic artery, the renal artery and the left iliac artery.

description of the mesh partition can be found in Barker and Cai [6].

2.2. Governing equations

We model the blood as a Newtonian flow and consider the following 3D unsteady incompressible Navier-Stokes equations,

$$\begin{cases} \rho\left(\dfrac{\partial \boldsymbol{u}}{\partial t} + (\boldsymbol{u}\cdot\nabla)\boldsymbol{u}\right) - \nabla\cdot\boldsymbol{\sigma} &= 0, \quad in \quad \Omega\times(0,T], \\ \nabla\cdot\boldsymbol{u} &= 0, \quad in \quad \Omega\times(0,T], \end{cases} \tag{1}$$

where $\boldsymbol{u}$ is the velocity vector, ρ is the blood density, and $\boldsymbol{\sigma}$ is the Cauchy stress tensor defined as

$$\boldsymbol{\sigma} = -p\boldsymbol{I} + 2\mu\boldsymbol{\varepsilon}(\boldsymbol{u}),$$

with p being the pressure, $\boldsymbol{I}$ being the 3×3 identity tensor, μ being the dynamic viscosity and $\boldsymbol{\varepsilon}(\boldsymbol{u})$ being the deformation tensor calculated by $\boldsymbol{\varepsilon}(\boldsymbol{u}) = 1/2(\nabla\boldsymbol{u} + \nabla\boldsymbol{u}^T)$. The initial condition is imposed as

$$\boldsymbol{u}|_{t=0} = \boldsymbol{u}_0, \quad in \quad \Omega.$$

Different boundary conditions are applied. Specifically, Dirichlet boundary conditions are imposed on the inlet and wall boundaries,

$$\begin{cases} \boldsymbol{u} = \boldsymbol{v}_I, & on \quad \Gamma_I\times(0,T], \\ \boldsymbol{u} = 0, & on \quad \Gamma_W\times(0,T], \end{cases}$$

where $\boldsymbol{v}_I$ is a plug flow velocity calculated from the profile of the patient-specific pulsatile flow rate measured clinically, as shown in Fig. 3 $\rho = 1.06$ g/cm^3 and $\mu = 0.035$ g/cm $\cdot$ s are used to characterize the properties of the blood. Let D be the diameter of the inlet, then the Reynolds number is $\mathrm{Re} = \rho D|\boldsymbol{v}_I|/\mu$, whose range is (4, 3185) due to the change of the velocity.

We investigate two types of outlet boundary conditions including the popularly used traction-free boundary condition and the resistance boundary condition to all outlet boundaries [49]. For the traction-free boundary condition, the outlet surface is free from the external stress, i.e.,

$$\boldsymbol{\sigma}_i\cdot\boldsymbol{n}_i = 0, \quad on \quad \Gamma_{O_i}\times(0,T], \ i = 1,2,\ldots m,$$

where $\boldsymbol{\sigma}_i$ is the previously defined Cauchy stress tensor and $\boldsymbol{n}_i$ is the outward normal of the ith outlet. For the resistance boundary condition, the pressure and the flow rate imposed at the ith outlet are related according to

$$p_i = R_iQ_i, \quad on \quad \Gamma_{O_i}\times(0,T], \ i = 1,2,\ldots m,$$

where R_i and Q_i are the resistance and the flow rate at the ith outlet, and $Q_i = \int_{\Gamma_{O_i}}\boldsymbol{u}\cdot\boldsymbol{n}_i ds$ [49]. For each simulation, a total resistance R is chosen and R_i is then determined by $R_i = R\sum_{i=1}^{m}S_i^{3/2}/S_i^{3/2}$, where S_i is the area of the ith outlet surface [28].

2.3. Stabilized finite element discretization

Consider the following trial and weight function spaces

$$\begin{aligned} V &:= \left\{\boldsymbol{u}\in\left[H^1(\Omega)\right]^3, \boldsymbol{u} = \boldsymbol{v}_I on\Gamma_I and \boldsymbol{u} = 0 on\Gamma_w\right\}, \\ V^0 &:= \left\{\boldsymbol{u}\in\left[H^1(\Omega)\right]^3, \boldsymbol{u} = 0 on(\Gamma_i\cup\Gamma_w)\right\}, \\ P &:= \left\{p\in L^2(\Omega)\right\} \end{aligned}$$

Then the weak form of Eq. (1) is: find $\boldsymbol{u}\in V$ and $p\in P$ such that $\forall\boldsymbol{\phi}\in V^0$ and $\forall\psi\in P$,

$$\mathcal{B}_f(\{\boldsymbol{u},p\},\{\boldsymbol{\phi},\psi\}) = 0,$$

where

$$\mathcal{B}_f(\{\boldsymbol{u},p\},\{\boldsymbol{\phi},\psi\}) = \rho\int_\Omega \frac{\partial \boldsymbol{u}}{\partial t}\cdot\boldsymbol{\phi}d\Omega + \rho\int_\Omega (\boldsymbol{u}\cdot\nabla)\boldsymbol{u}\cdot\boldsymbol{\phi}d\Omega - \int_\Omega p(\nabla\cdot\boldsymbol{\phi})d\Omega + 2\mu\int_\Omega \boldsymbol{\varepsilon}(\boldsymbol{u}):\boldsymbol{\varepsilon}(\boldsymbol{\phi})d\Omega + \int_\Omega (\nabla\cdot\boldsymbol{u})\psi d\Omega + \int_{\Gamma_o}(\boldsymbol{\sigma}\cdot\boldsymbol{n})\cdot\boldsymbol{\phi}ds. \quad (2)$$

Unlike the traction-free boundary condition $\boldsymbol{\sigma}\cdot\boldsymbol{n} = 0$, which means the last term in Eq. (2) can be neglected, the resistance boundary condition implies a boundary integral term [51].

$$\int_{\Gamma_o}(\boldsymbol{\sigma}\cdot\boldsymbol{n})\cdot\boldsymbol{\phi}ds = \sum_{i=1}^{m}\int_{\Gamma_{o_i}}\left(-R_i\int_{\Gamma_{o_i}}\boldsymbol{u}\cdot\boldsymbol{n}_i ds\boldsymbol{I} + 2\mu\boldsymbol{\varepsilon}(\boldsymbol{u})\right)\cdot\boldsymbol{n}_i\cdot\boldsymbol{\phi}ds.$$

For the spatial discretization of Eq. (2), we use P_1–P_1 finite elements. However, additional stabilization terms are required, since this finite element pair does not satisfy the Ladyzhenskaya-Babuška-Breezi (LBB) condition. In this work, we adopt the streamline upwind Petrov Galerkin method. Denoting the finite element subspaces as V_h, V_h^0 and P_h corresponding to their infinite dimensional spaces, we present the following semi-discrete formulation to the above weak form: find $\boldsymbol{u}_h \in V_h$ and $p_h \in P_h$, such that $\forall\boldsymbol{\phi}_h \in V_h^0$ and $\forall\psi_h \in P_h$,

$$\mathcal{B}(\{\boldsymbol{u}_h,p_h\},\{\boldsymbol{\phi}_h,\psi_h\}) = \mathcal{B}_f(\{\boldsymbol{u}_h,p_h\},\{\boldsymbol{\phi}_h,\psi_h\}) + \sum_{K\in\Omega_h}(\nabla\cdot\boldsymbol{u},\tau_a\nabla\cdot\boldsymbol{\phi})_K + \sum_{K\in\Omega_h}\left(\frac{\partial \boldsymbol{u}_h}{\partial t} + (\boldsymbol{u}_h\cdot\nabla)\boldsymbol{u}_h + \nabla p_h, \tau_b(\boldsymbol{u}_h\cdot\nabla\boldsymbol{\phi}_h + \nabla\psi_h)\right)_K + \sum_{K\in\Omega_h}(\bar{\boldsymbol{u}}_h\cdot\nabla\boldsymbol{u}_h,\boldsymbol{\phi}_h)_K + \sum_{K\in\Omega_h}(\bar{\boldsymbol{u}}_h\cdot\nabla\boldsymbol{u}_h,\tau_c\bar{\boldsymbol{u}}_h\cdot\nabla\boldsymbol{\phi}_h)_K,$$

where $\Omega_h = \{K\}$ is the unstructured tetrahedral mesh. For the definition of $\bar{\boldsymbol{u}}_h$ and the suggested values of stabilization parameters τ_a, τ_b and τ_c, we refer to Wu and Cai [52] and Kong et al. [25].

After the spatial discretization, we obtain a time-dependent semi-discretized nonlinear system

$$\frac{d\mathcal{X}(t)}{dt} = \mathcal{N}(\mathcal{X}(t)),$$

where $\mathcal{N}(\mathcal{X}(t))$ is a nonlinear algebraic function of $\mathcal{X}$ and $\mathcal{X}(t)$ is a time-dependent solution vector for the nodal values of both velocity $\boldsymbol{u}_h$ and pressure p_h at time t. We then employ an implicit backward Euler method to the time direction and obtain the following fully discretized system [52].

$$\mathcal{X}_n - \mathcal{X}_{n-1} = \Delta t\mathcal{N}(\mathcal{X}_n),$$

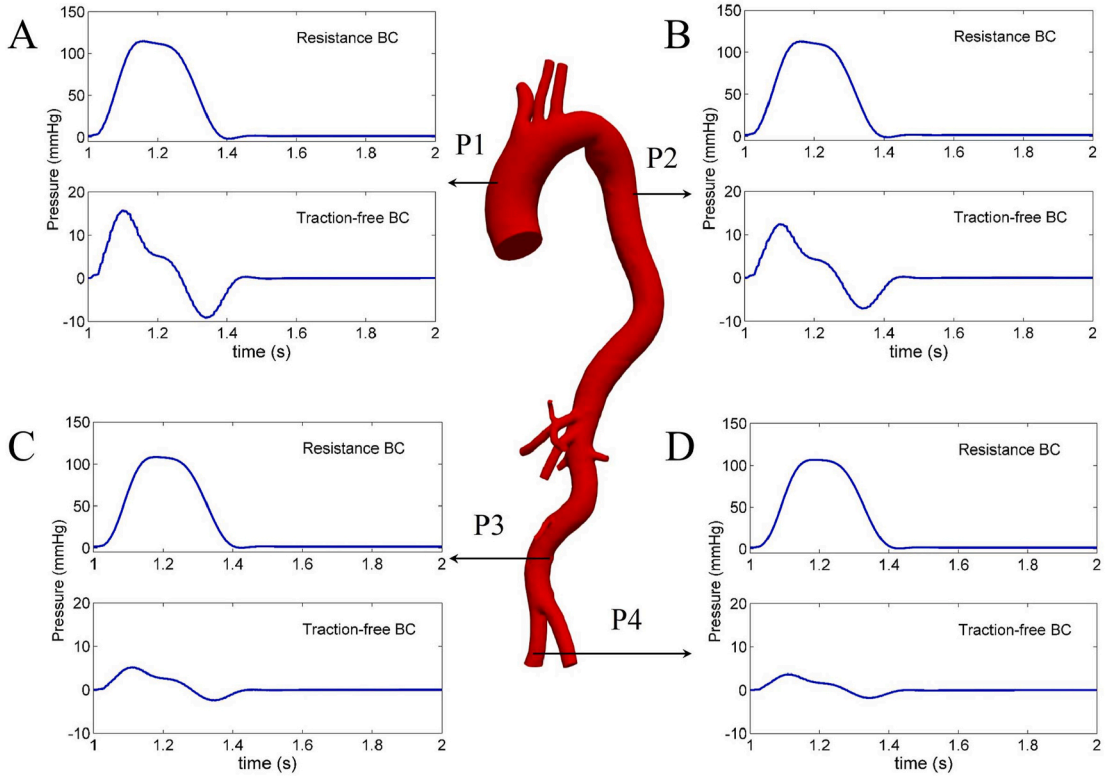

Fig. 5. A comparison of computed pressure values with the resistance and traction-free boundary conditions for four points: (A) *P*1 in the ascending aorta, (B) *P*2 in the thoracic aorta, (C) *P*3 in the abdominal aorta and (D) *P*4 in the common iliac.

where Δt is the time-step size and $\mathcal{X}_n$ denotes the solution vector at the nth time step. The initial guess $\mathcal{X}_0$ is often assumed to be zero. Thus, the problem is transferred into solving the following large, sparse and nonlinear algebraic system at every time step

$$\mathcal{F}(\mathcal{X}_n) = 0. \tag{3}$$

2.4. Newton-Krylov-Schwarz algorithm

We next describe the Newton-Krylov-Schwarz (NKS) method for solving Eq. (3). This method comprises three parts: an inexact Newton method to handle the nonlinearity of the system; a Krylov subspace method to deal with the linear Jacobian system within each Newton step; and a Schwarz preconditioner to accelerate the Jacobian solver. The overall computational framework is summarized in Algorithm 1.

Algorithm 1. Newton-Krylov-Schwarz

Set the convergence tolerance for the absolute error ϵ_a and the relative error ϵ_r;
for each time step $n = 1, 2, \cdots$, **do**
  Choose the initial guess for Newton iteration as $\mathcal{X}_n^0 = \mathcal{X}_{n-1}$;
  for each Newton step $k = 1, 2, \cdots$, **do**
    if $\|\mathcal{F}(\mathcal{X}_n^k)\| < \epsilon_a$ or $\|\mathcal{F}(\mathcal{X}_n^k)\| < \epsilon_r \|\mathcal{F}(\mathcal{X}_n^0)\|$ **then**
      Break;
    end if
    Construct the Jacobian matrix J_n^k and setup the restricted additive Schwarz preconditioner $(M_n^k)^{-1}$;
    Compute the Newton correction step S_n^k by solving the preconditioned Jacobian system until it satisfies $\|J_n^k (M_n^k)^{-1} M_n^k S_n^k + \mathcal{F}(\mathcal{X}_n^k)\| \le \eta^k \|\mathcal{F}(\mathcal{X}_n^k)\|$;
    Calculate the step size τ_n^k by a cubic linesearch;
    Update the solution with $\mathcal{X}_n^{k+1} = \mathcal{X}_n^k + \tau_n^k S_n^k$;
  end for
  Store the converged $\mathcal{X}_n^{k+1}$ as the solution $\mathcal{X}_n$;
end for

The inexactness of the inexact Newton method is controlled by the forcing term η^k. If taking $\eta^k = 0$, the inexact Newton method becomes the Newton method. For the Newton type methods, one can use an approximate or an exact Jacobian matrix. In this work, the analytically computed exact Jacobian is used since it offers better computational performance than the approximate Jacobian [6,10].

Within each Newton step, the Jacobian system is inexactly solved by using a Krylov subspace method, the generalized minimal residual method (GMRES). To accelerate the GMRES convergence, we apply an additive Schwarz preconditioner. For simplicity, we drop the subscript and superscript and rewrite the restricted additive Schwarz preconditioner $(M_n^k)^{-1}$ as M^{-1} and the Jacobian matrix J_n^k as J. To define M^{-1}, we extend the subdomain Ω_h^l into an overlapping subdomain $\Omega_h^{l,\delta}$ such that

$$\Omega_h = \bigcup_{l=1}^{N} \Omega_h^{l,\delta},$$

where the integer $\delta > 0$ is the overlapping size of a subdomain with its adjacent subdomains. Denote the restriction operator R_l^δ that extracts from the global vector to the local vector of unknowns corresponding to the overlapping subdomain $\Omega_h^{l,\delta}$ and the prolongation operator $(R_l^\delta)^T$, namely the transpose of the restriction operator, that maps the local vector of unknowns to the global domain. Similarly, we denote R_l^0 and $(R_l^0)^T$ as the restriction and prolongation operators of the non-overlapping subdomain Ω_h^l. Thus, we define the restricted additive Schwarz preconditioner without the super and subscripts as [26].

$$M^{-1} = \sum_{l=1}^{N} (R_l^0)^T B_l^{-1} R_l^\delta,$$

where B_l^{-1} is the inverse of the overlapping subdomain Jacobian matrix given by $B_l = R_l^\delta J (R_l^\delta)^T$ and the matrix-vector multiplication ($B_l^{-1} v$ for any subdomain vector v) needed in the preconditioning operations can be carried out by solving approximately by the incomplete LU factorization (ILU) with certain level of fill-ins. The preconditioner is reconstructed at every Newton iteration, and so are the ILU factorizations of the subdomain matrices.

The method described in this section is implemented using the Portable Extensible Toolkit for Scientific computing (PETSc) library [5]. If not specifically mentioned, the linear solver stops when the relative error reaches 10^{-3} and the nonlinear solver stops when the absolute or relative error reaches 10^{-6}. Apart from the flow rate, the pressure and the velocity, we also focus on the analysis of the WSS and the oscillatory shear index (OSI), which are important hemodynamic parameters for the clinical investigation of the aortic aneurysm. The WSS is defined by the difference between the overall shear stress and its normal projection [25],

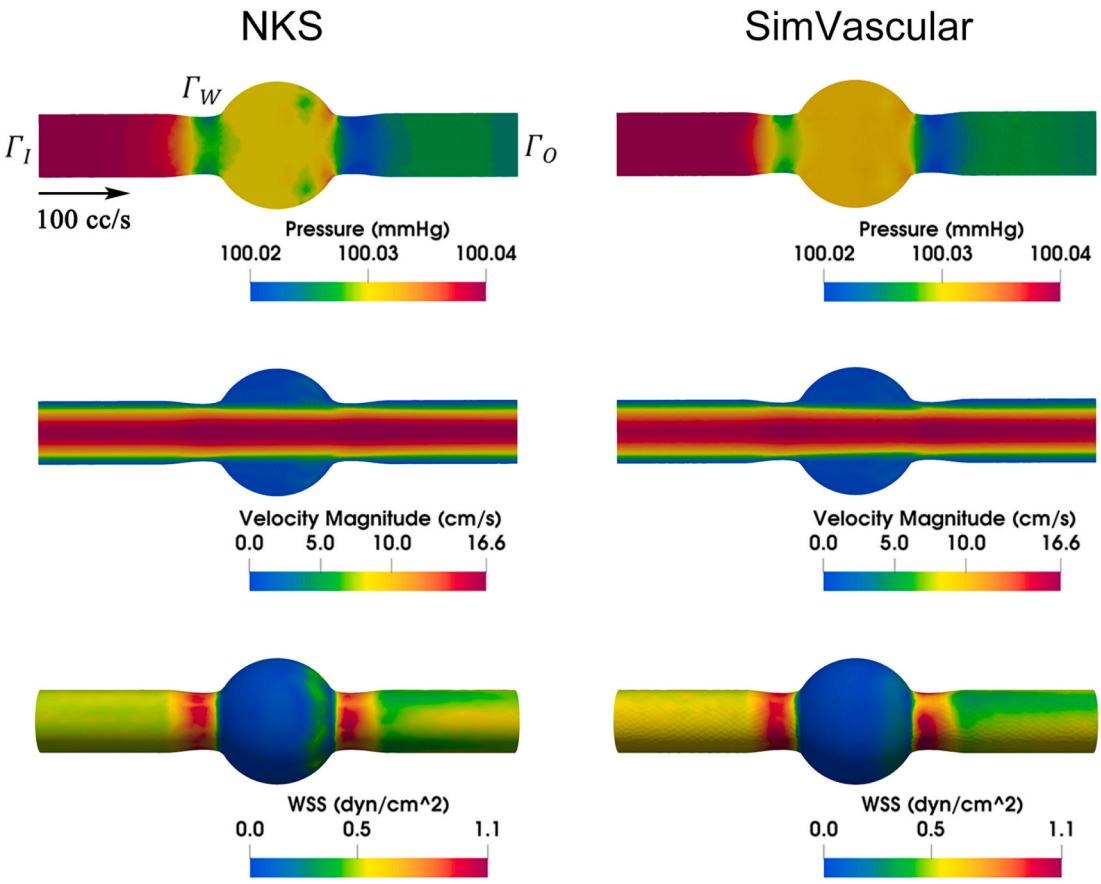

Fig. 6. The distributions of the pressure, velocity and wall shear stress computed with Newton-Krylov-Schwarz (NKS) and SimVascular.

Table 2
The comparison of the maximum, minimum and average values of the pressure (*mmHg*), velocity (*cm/s*) and wall shear stress (dyn/cm^2) computed with Newton-Krylov-Schwarz (NKS) method and SimVascular.

	Number of elements	P_{max}	P_{min}	P_{ave}	V_{max}	V_{min}	V_{ave}	WSS_{max}	WSS_{min}	WSS_{ave}
NKS	130522	100.042	100.017	100.030	17.303	0.000	5.303	1.104	0.001	0.360
SimVascular	130820	100.045	100.015	100.032	17.138	0.000	5.109	1.156	0.001	0.369

Table 3
The surface-averaged pressure (*mmHg*) and magnitude of the wall shear stress (dyn/cm^2), and the space-averaged magnitude of the velocity (*cm/s*) obtained using meshes with different number of elements.

Number of elements	Pressure t = 1.1*s*	Pressure t = 1.2*s*	Pressure t = 1.3*s*	Velocity t = 1.1*s*	Velocity t = 1.2*s*	Velocity t = 1.3*s*	WSS t = 1.1*s*	WSS t = 1.2*s*	WSS t = 1.3*s*
1.11×10^6	77.83	110.82	71.17	20.51	36.64	27.79	8.62	11.70	7.89
3.99×10^6	77.19	110.23	71.07	20.51	36.62	27.79	11.89	15.37	10.04
7.35×10^6	76.99	110.14	71.03	20.55	36.67	27.82	14.61	18.28	11.52
30.02×10^6	76.79	110.96	70.93	20.34	36.57	27.90	18.53	22.05	13.40

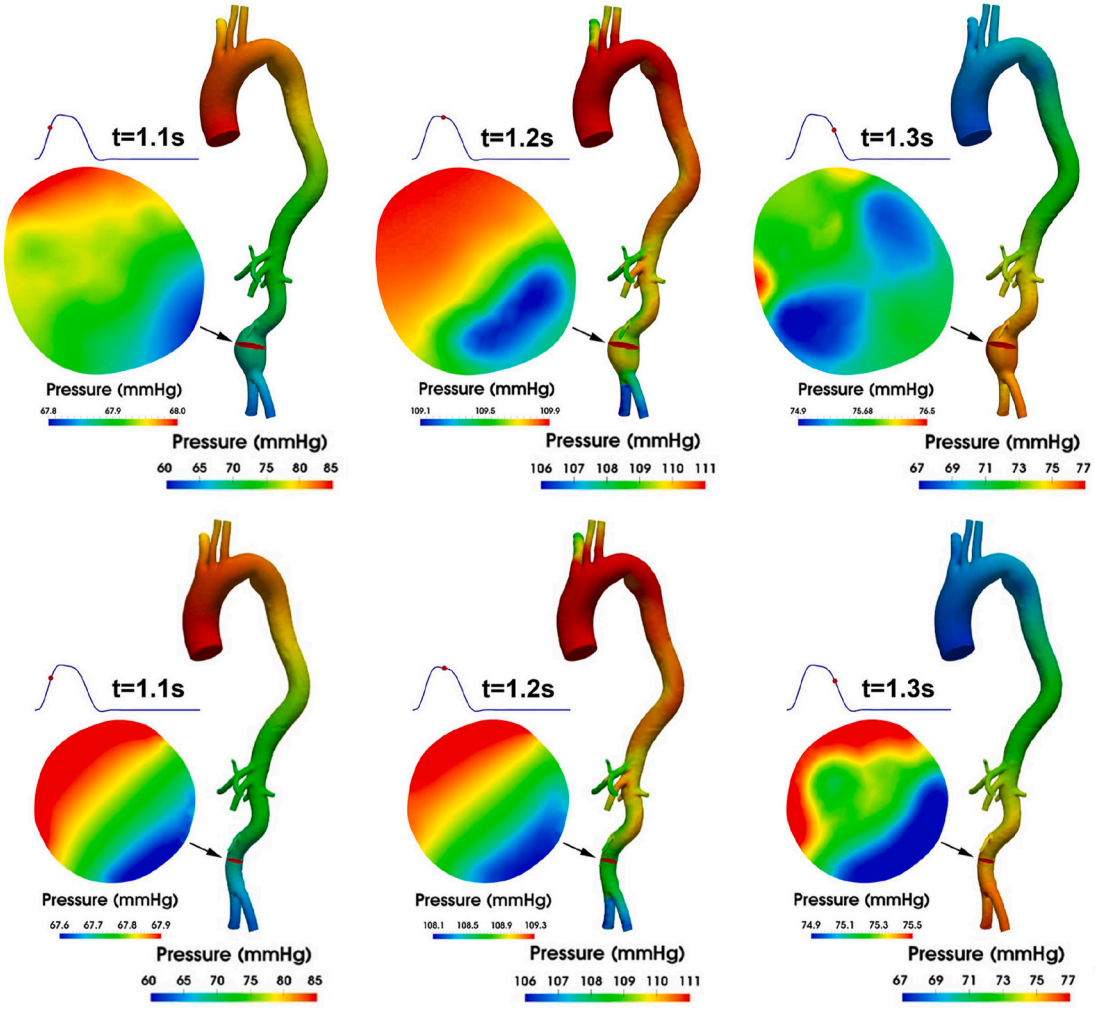

Fig. 7. The computed pressure distribution and the pressure distribution at a cross section of pre- and post-operative abdominal aortas at $t = 1.1\ s$, $1.2s$ and $1.3s$ during the early, mid and late systole.

$$WSS = \boldsymbol{\sigma n}_p - (\boldsymbol{\sigma n}_p \cdot \boldsymbol{n}_p)\boldsymbol{n}_p,$$

where $\boldsymbol{n}_p$ is the normal vector at a point on the wall. The OSI is defined by Ref. [11].

$$OSI = \frac{1}{2}\left(1 - \frac{\left|\int_0^T WSS dt\right|}{\int_0^T |WSS| dt}\right)$$

3. Results and discussions

3.1. Pulsatile flows in a patient-specific abdominal artery

As we have already mentioned, two types of boundary conditions for the outlets are considered, namely the traction-free and the resistance boundary conditions. For the resistance boundary condition, a total resistance of $R = 500\ \text{dyn} \cdot s \cdot cm^{-5}$ is prescribed to make sure the computed maximum pressure matches the systolic blood pressure measured for the patient. Fig. 4 compares the computed flow rate from the resistance and the traction-free boundary conditions for four branches, namely the left subclavian artery, the splenic artery, the renal artery and the left iliac artery. Here, the simulation is conducted on the post-operative case with a mesh of 8.14×10^5 nodes and 3.99×10^6 elements. The time-step size is set to be 0.004 s. With the resistance boundary condition, the outflow rate profiles agree with the inflow rate waveform, which is consistent with the results reported in Reymond et al. [43]. However, in the case of the traction-free boundary condition, it shows physiologically unreasonable shape alterations. Fig. 5 further compares the resulting pressures between the resistance and traction-free boundary conditions at positions in different aortic regions: (A) $P1$ in the ascending aorta, (B) $P2$ in the thoracic aorta, (C) $P3$ in the abdominal aorta and (D) $P4$ in the common iliac. We see that both boundary conditions present a gradual decrease of the peak pressure as the blood travels from $P1$ to $P4$. Althogh the resistance boundary condition gives an unrealistically large pressure amplitude which can be rectified by adding a reference pressure, the traction-free boundary condition results in more unrealistic patterns with negative pressures, incorrect peak values and unreasonable oscillations. These findings confirm that the choice of outlet boundary conditions makes a remarkable difference on the calculated results; and the resistance boundary condition outperforms the traction-free boundary condition in achieving more physiologically relevant results [49].

For the rest of the paper we focus only on the resistance boundary condition. We provide a validation of the proposed method by a comparison with SimVascular [47]. As shown in Fig. 6, we consider an idealized cylindrical vessel with radius 2 cm and length 30 cm connected smoothly with a spherical aneurysm of radius 4 cm in the middle. We prescribe a constant volumetric inflow rate of 100 cc/s with a parabolic

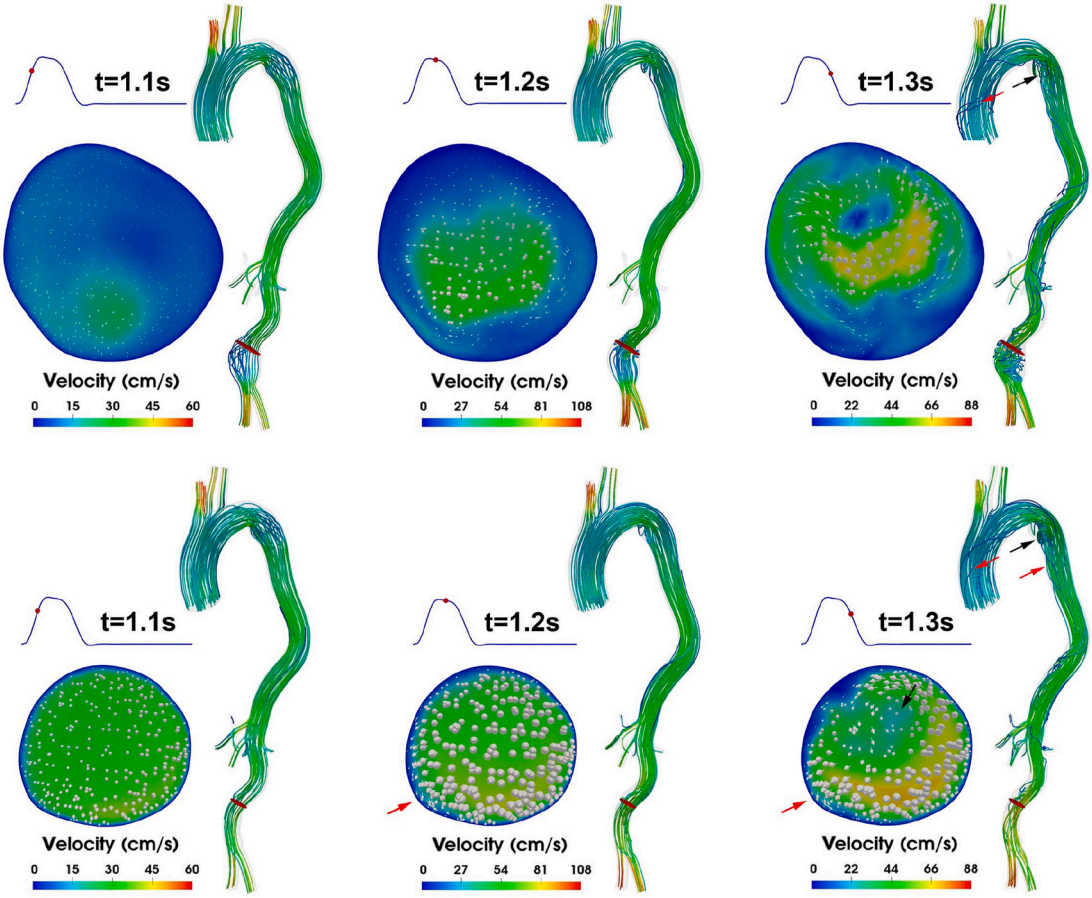

Fig. 8. The streamlines of velocity field and the velocity at a cross section of pre- and post-operative abdominal aortas at $t = 1.1\ s$, $1.2\ s$ and $1.3\ s$, namely during the early, mid and late systole respectively. The velocity vector in the cross section is represented by the size and direction of the arrow with a bottom-up view. The black and red arrows show the locations of vortex and secondary flows.

profile at the inlet and a resistance of 1333 $\text{dyn} \cdot s \cdot cm^{-5}$ at the outlet. To achieve the steady state, a time-step size 0.03 s is used and the total number of steps is 200. For SimVascular, the mesh has 130820 elements, the nonlinear solver converges with a tolerance 1×10^{-2} and the linear solver converges with tolerances 5×10^{-2} for the momentum equation and 4×10^{-1} for the continuity equation. For NKS, the mesh has 130522 elements and the experiment is carried out using 24 CPU cores. The overlapping size between the neighbouring subdomains is 3 and the ILU fill-in level is 3. We compare the maximum, minimum and average values of the pressure (P_{max}, P_{min}, P_{ave}), velocity (V_{max}, V_{min}, V_{ave}) and wall shear stress (WSS_{max}, WSS_{min}, WSS_{ave}), as listed in Table 2. We also show the distributions of the pressure, velocity and WSS obtained from NKS and SimVascular in Fig. 6. It can be seen that these quantities match quite well.

To ensure the accuracy of the simulation, we consider the mesh-dependence of the numerical solution for the post-operative case. Four finite element meshes with 1.11×10^6, 3.99×10^6, 7.35×10^6 and 30.02×10^6 elements are used. As shown in Table 3, an increase in the number of elements improves the accuracy of all quantities and a mesh with 1.11×10^6 elements can provide mesh-independent pressure and velocity, but fails to provide a point-wise converged WSS. With the 30.02×10^6 element mesh, we are able to capture the distribution pattern of the WSS, though the accuracy of the point-wise values can be further improved by a finer mesh [56]. Note that for the 30.06×10^6 element mesh, the mean size of the surface elements is about 0.16 mm, which is higher than the resolution of 4D MRI that is around 2.5 mm in Ref. [57].

Fig. 7 shows the pressure distribution of the pre- and post-operative aortas, calculated using the 4.04×10^6 and 3.99×10^6 element meshes respectively, at three different times $t = 1.1s$, $1.2s$ and $1.3s$ during the early, mid and late systole correspondingly. For both cases, we see that the pressure varies both temporally and spatially. Temporally, the pressure profile at $t = 1.3s$ is distinct from what appears at $t = 1.1\ s$ and $1.2\ s$, which may be closely related to the velocity propagation. Spatially, the pressure varies in the abdominal section due to the change of geometry by the aneurysm repair. In the same figure, we also show the abdominal pressure variations in the cross section plane, where higher average pressures 67.91, 109.61 and 75.45 mmHg are found at the cross section of the pre-operative case comparing to 67.79, 108.83 and 75.20 mmHg in the post-operative case at $t = 1.1s$, $1.2s$ and $1.3s$ respectively. Therefore, we conclude that the pressure is reduced by the aneurysm repair, which is consistent with the results reported in Ref. [44].

Based on the same meshes for the pressure, Fig. 8 presents the streamlines of the velocity field and the velocity in a cross section for the pre- and post-operative cases at $t = 1.1\ s$, $1.2\ s$ and $1.3\ s$. For both cases, we observe that physiologically reasonable values of velocity magnitude are obtained that are similar to the published results in Ref. [38]. Moreover, relatively stable streamline patterns can be seen at the early and mid systole, but become unstable at the late systole, which is consistent with the results reported in Youssefi et al. [53]. Besides, the secondary flow motion in the vicinity of the artery wall (the red arrows) and the vortex flow along the lesser aortic curvature (the black arrows) are observed, especially during the late systole [46]. In the abdominal cross-sectional plane, the velocity vector is represented by the size and direction of the arrow with a bottom-up view. It shows that the velocity

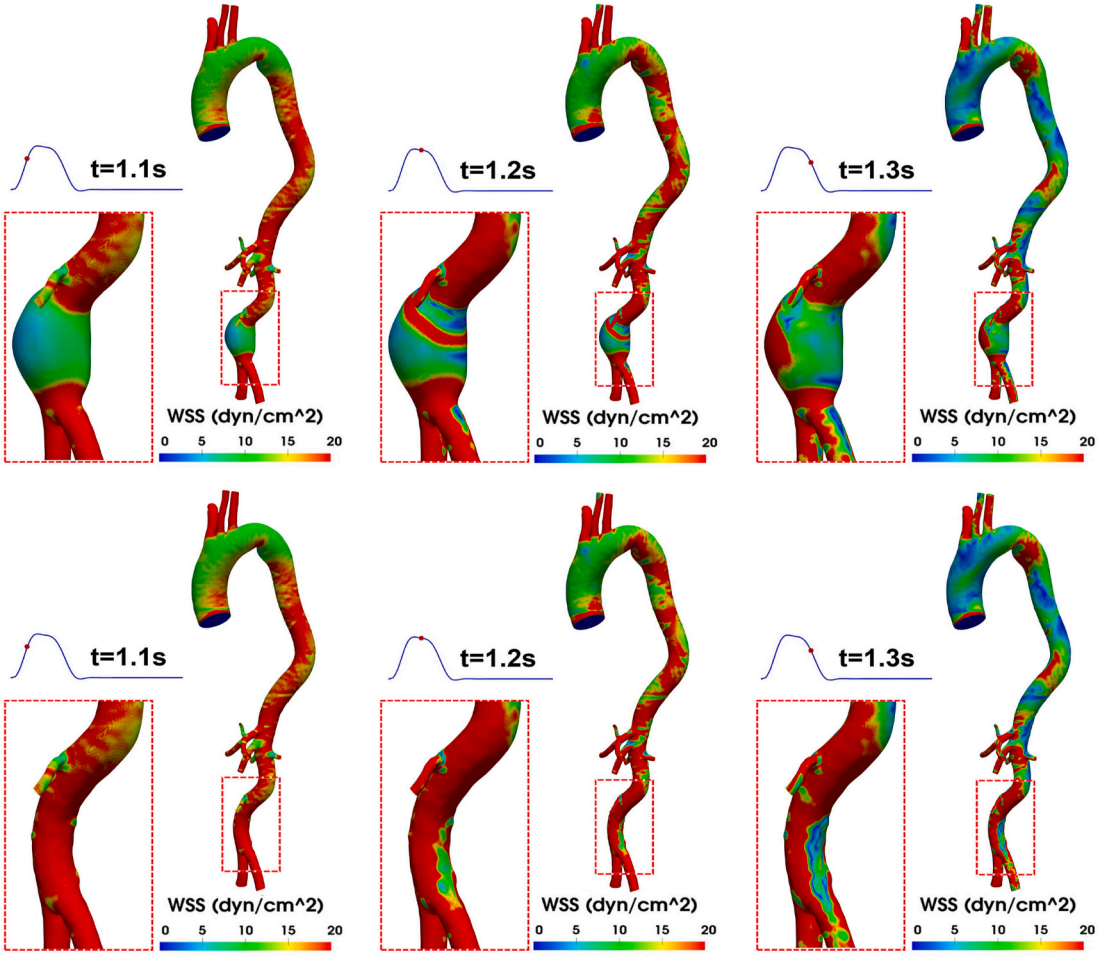

Fig. 9. The magnitude of the wall shear stress at $t = 1.1\ s$, $1.2\ s$ and $1.3\ s$ of the pre- and post-operative abdominal aortas during the early, mid and late systole. The dotted box area of the abdominal aorta is an magnified view to show the distribution of the wall shear stress.

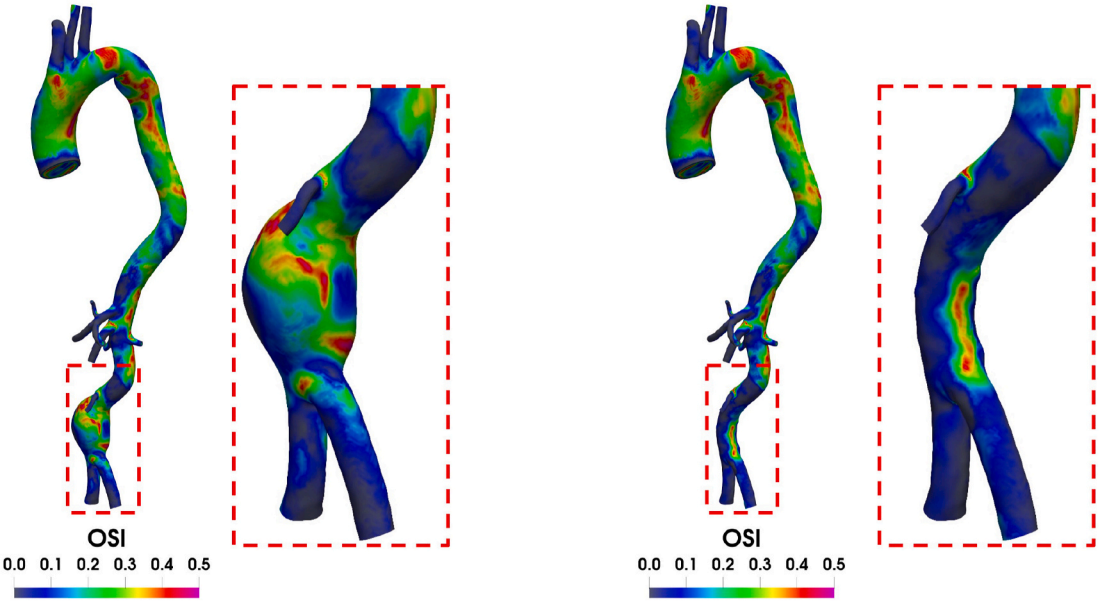

Fig. 10. The spatial distributions of OSI of the pre- and post-operative abdominal aortas. Zoom-in views in the dotted boxes present the OSI distributions in the area of the aneurysm.

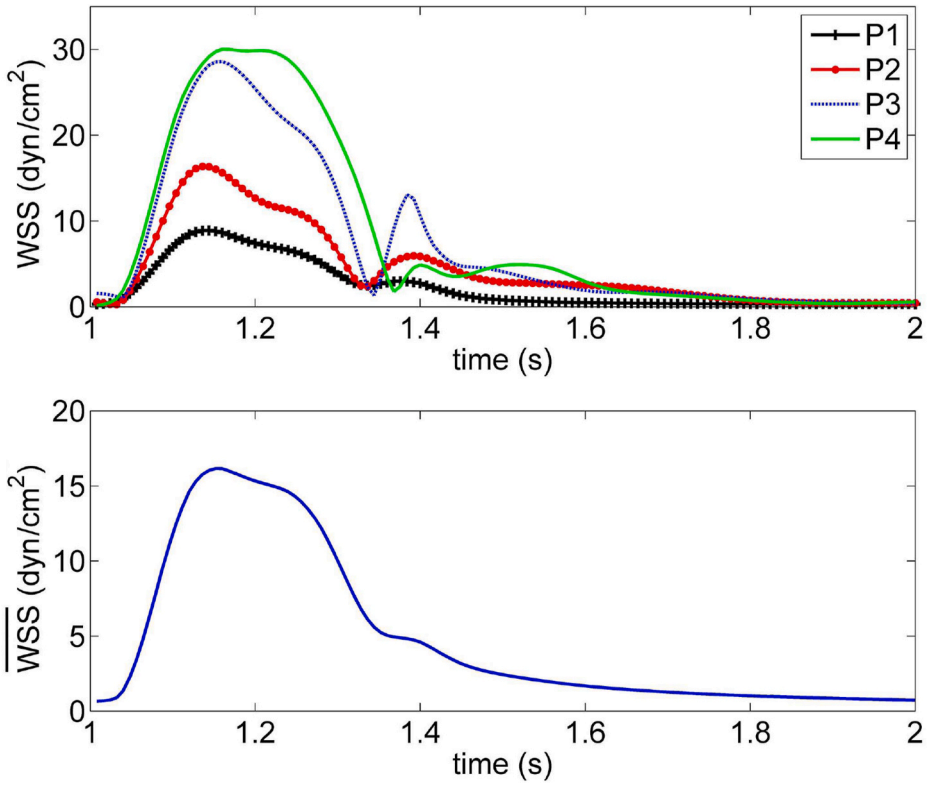

Fig. 11. The temporal changes of the wall shear stress at 4 different points $P1$, $P2$, $P3$ and $P4$ in Fig. 5 and the surface-averaged wall shear stress $\overline{WSS}$ for a cardiac cycle.

Table 4
The influence of the overlapping size $\delta = 4, 6, 8, 10$ and the subdomain solvers with fill-in level $l = 1, 2, 3, 4$. The simulation is conducted on the post-operative case with a mesh consisting of 3.99×10^6 elements for 10 time steps with a step size 0.001 s.

Subsolver	δ	Newton	GMRES	Time (s)	Memory (M)
ILU(1)	4	2.10	532.95	37.50	1014.48
	6	2.10	464.24	34.90	1207.18
	8	2.20	354.18	31.16	1544.59
	10	2.20	335.05	33.15	1937.76
ILU(2)	4	2.10	495.48	42.70	1406.29
	6	2.20	373.41	36.71	1742.80
	8	2.20	179.23	22.48	2170.21
	10	2.20	171.77	24.61	2741.67
ILU(3)	4	2.10	327.67	37.00	1881.75
	6	2.10	177.38	24.28	2277.50
	8	2.10	125.95	21.65	2863.54
	10	2.10	112.29	23.66	3644.95
ILU(4)	4	2.10	323.57	45.33	2445.86
	6	2.10	163.90	29.17	2978.56
	8	2.10	97.71	24.87	3791.81
	10	2.10	96.71	30.07	4866.35

is unevenly distributed for both the pre- and post-operative cross sections, where lower average velocities 10.39, 24.66 and 28.78 cm/s are found at the cross section of the pre-operative case comparing to 27.21, 52.16 and 40.58 cm/s in the post-operative case at $t = 1.1s$, $1.2s$ and $1.3s$ respectively. We also find that the geometric variation has a great influence on the flow field so that the chaotic streamlines in the aneurysm become laminar after the surgical repair, especially at the late systole [45].

Fig. 9 shows the profiles of the magnitude of the WSS computed with 30.06×10^6 and 30.02×10^6 element meshes for the pre- and post-operative cases respectively. For both cases, we see that the adopted meshes are adequate to capture the complex patterns of the WSS, which is unevenly distributed and shows reasonable values comparing to that reported in Ref. [12]. Patches with higher values of WSS are observed at the inner side rather than the outer side of the aortic arch and its three major branches, similar results were reported in Lantz et al. [29]. Actually, for a specific time, both cases show the same WSS distribution except in the abdominal section, where the geometry is changed. Magnified images are presented to show the detailed WSS distributions in the dotted box area of the abdominal aorta at three different times. For both cases, the instantaneous WSS patterns are significantly different in the abdominal section. For the pre-operative case, it shows a lower magnitude of WSS comparing to the post-operative case and irregular patches of low WSS exist at $t = 1.2$ s and $t = 1.3$ s in the abdominal aneurysm wall. However, for the post-operative case, the abdominal part of the aorta is subjected to high values of WSS and the low WSS patches appear only at $t = 1.3$ s, probably because of the geometric bends and bifurcations. Boyd et al. [8] and Zambrano et al. [54] showed that the low WSS has been correlated with the thrombus deposition and the aneurysmal expansion. Meyrignac et al. corroborated these findings and reported its association with the aneurysmal growth and rupture [34]. Fortunately, our study shows the aneurysm repair can successfully increase the magnitude of the WSS.

Due to the pusatile nature of the inflow rate, the WSS vector presents directional changes during a cardiac cycle with the degree quantified by a dimensionaless metric OSI. From its definition, the value of OSI ranges from 0.0 in an unidirectional flow to 0.5 in a reversing flow with no preferred directions. Fig. 10 shows the spatial distributions of OSI of the pre- and post-operative abdominal aortas. Overall, our results show expected values of OSI ranging from 0.0 to 0.5 and are coherent with the findings that high values of OSI are located at sites where acute geometric changes occur, including bifurcations and high curvatures [41]. This may explain the fact that the aortic dissections and aneurysms are

Table 5
Parallel performance using different number of processor cores with $\delta = 8$ and $l = 3$. Three meshes with 4.04×10^6, 7.55×10^6 and 30.06×10^6 elements for the pre-operative case and three meshes with 3.99×10^6, 7.35×10^6 and 30.02×10^6 elements for the post-operative case are tested.

Case	Mesh	*np*	Newton	GMRES	Time (*s*)	Memory (*M*)	Speedup	Efficiency
Pre-	4.04×10^6	120	2.1	128.62	65.81	8416.81	1.00	100%
		240	2.1	125.71	36.94	4907.13	1.78	89%
		480	2.1	120.10	21.87	1781.23	3.01	75%
	7.55×10^6	360	2.1	248.10	78.32	6323.81	1.00	100%
		720	2.1	128.68	44.13	3050.61	1.77	89%
		1440	2.1	172.57	23.94	1776.58	3.27	82%
	30.06×10^6	720	2.1	444.58	232.27	9839.44	1.00	100%
		1440	2.1	414.11	122.70	6055.46	1.89	95%
		2880	2.1	431.53	86.91	2909.31	2.67	67%
Post-	3.99×10^6	120	2.1	127.52	63.37	7377.61	1.00	100%
		240	2.1	131.24	37.17	4369.27	1.70	85%
		480	2.1	125.95	21.65	2863.54	2.93	73%
	7.35×10^6	360	2.1	244.81	72.16	5102.98	1.00	100%
		720	2.1	198.29	38.66	2978.35	1.87	93%
		1440	2.1	182.62	23.88	1743.44	3.02	76%
	30.02×10^6	720	2.1	431.26	236.53	9816.90	1.00	100%
		1440	2.1	450.47	140.82	5688.60	1.68	84%
		2880	2.1	410.37	86.66	3093.55	2.73	68%

typically developed at the aortic arch and the abdominal aorta where the high osccilation of WSS imposes a tearing effect on the inner endothelial cells of the arterial wall. Like the WSS, differences of OSI between the two cases are observed in the abdominal section where the geometrical changes occur, as shown in the zoom-in views. Boyd et al. [8] showed that rupture occurs in or near the patches of high-value OSI where the flow recirculates, which are significantly removed after the aneurym repair. The lower values of OSI indicates that the reversing flow becomes laminar in the abdominal region after the aneurysm repair, as also indicated by the streamlines of the velocity in Fig. 8.

We also plot the temporal variation of the point-wise and the surface-averaged WSS based on the post-operative abdominal aorta in Fig. 11.

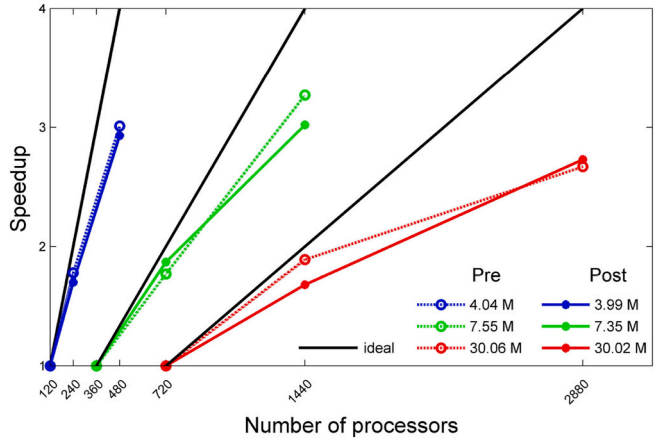

Fig. 12. The speedup versus the number of processor cores for the pre- and post-operative abdominal aortas, where the pre-operative case with 4.04×10^6, 7.55×10^6 and 30.06×10^6 elements and the post-operative case with 3.99×10^6, 7.35×10^6 and 30.02×10^6 elements. The overlapping size is $\delta = 8$ and subdomain solver is ILU(3). The solid black lines are for the ideal linear speedup.

Here, to save the computational time, we use a mesh with 3.99×10^6 elements to show a general trend of the variation of the WSS. For the point-wise WSS, four different points $P1$, $P2$, $P3$ and $P4$ in Fig. 5 are monitored. It shows that the WSS presents different profiles at these points. For the surface-averaged WSS, it is denoted as $\overline{WSS}$ and given by

$$\overline{WSS} = \frac{1}{A}\int_{\partial\Omega} WSS dA,$$

where A is the total surface area of the computational domain. It can be seen that the profile of the $\overline{WSS}$ is temporally correlated with the pulsatile inflow rate and its shape maintains a pulsatile form but with a relatively gentle downward slope.

3.2. Scalability and robustness

Now we study the scalability of the parallel algorithm and its robustness with respect to several important parameters for the pre- and post-operative aorta. It is noted that these parameters accelerate the convergence of the solver without impairing the accuracy. We first mention some notations to be used in the tables. "Subsolver" denotes the type of solvers for the subdomain problems. "ILU(l)" denotes the ILU with l level of fill-ins. "δ" denotes the overlapping size between the neighbouring subdomains. "Newton" means the average number of Newton iterations for each time step. "GMRES" stands for the average number of linear iterations for each Newton step. "Time" is the average wall clock time in seconds spent for each time step. "Memory" denotes the memory consumption per processor core in megabytes. "*np*" represents the number of processor cores, which equals to the number of subdomains denoted as N in the early sections of the paper. To measure the parallel performance of the algorithm when we increase the number of processor cores, we will use "speedup" and "parallel efficiency". For comparison, three base numbers of cores are considered with $np_0 = 120$, 360 and 720. Speedup is defined as the ratio of the compute times using

Table 6
The impact of time-step size Δt. The time-step sizes 1.00×10^{-3}, 5.00×10^{-3} and 1.00×10^{-2} are tested for the pre- and post-operative abdominal aortas with 120 and 360 cores.

Case	Mesh	*np*	Δt (*s*)	Newton	GMRES	Time (*s*)	Memory (*M*)
Pre-	4.04×10^6	120	1.00×10^{-3}	2.10	127.10	49.51	7377.61
			5.00×10^{-3}	3.10	326.87	195.77	12131.95
			1.00×10^{-2}	3.70	308.54	218.11	14361.03
	7.55×10^6	360	1.00×10^{-3}	2.10	172.57	23.94	1776.58
			5.00×10^{-3}	3.10	716.74	288.34	9150.69
			1.00×10^{-2}	3.70	347.78	175.93	10846.81
Post-	3.99×10^6	120	1.00×10^{-3}	2.10	125.10	63.02	7377.61
			5.00×10^{-3}	3.10	392.32	225.12	10598.93
			1.00×10^{-2}	3.60	231.56	161.19	12209.59
	7.35×10^6	360	1.00×10^{-3}	2.10	263.76	76.42	5102.98
			5.00×10^{-3}	3.20	682.44	262.39	7578.23
			1.00×10^{-2}	3.60	376.19	171.39	8478.33

the base number of cores and the compute time using *np* number of cores. Parallel efficiency is the speedup multiplied by np_0/np. GMRES is set to restart at every 500 iterations.

The impact of overlapping size and subdomain solver. The choices of the level of fill-in and the overlapping size make significant influences on the parallel performance of the algorithm. Table 4 shows the results obtained from the point-block ILU with $l = 1, 2, 3, 4$, and $\delta = 4, 6, 8, 10$. For this table, the simulation is carried out on the post-operative aorta for 10 time steps with a time step size 0.001 *s* on a mesh with 3.99×10^6 elements.

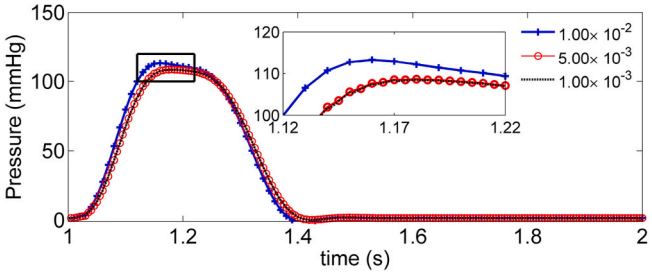

Fig. 13. The influence of the time-step sizes $\Delta t = 1.00 \times 10^{-3}$, 5.00×10^{-3} and $1.00 \times 10^{-2} s$ on the accuracy of the pressure at point *P*3.

δ is used to determine the amount of data that exchanges between the adjacent subdomains. A larger δ leads to a better perconditioner, which means fewer number of linear iterations. However, at the same time, a larger δ increases the communication cost. Hence, to minimize the total computing time, an appropriate δ should be chosen to balance the GMRES iterations and the communication cost. Specific for a fixed level of ILU fill-in in Table 4, the increase of δ from 4 to 8 reduces the computing time. A further increase of δ to 10 keeps reducing the GMRES iterations, but the averaged computing time tends to rise since the time saved by the reduction in linear iterations can not compensate for the extra communication cost. $\delta = 8$ offers the optimal performance in terms of the total computing time and is used in the following tests. It also shows that the memory requirement increases as δ becomes larger. Similarly, we face a trade-off for the ILU fill-in levels. For a fixed δ in Table 4, the memory requirement increases as l goes from 1 to 4. However, when l reaches 4, the number GMRES continues to reduce, but the computing time doesn't. Therefore, we set $l = 3$ for all the following experiments.

The parallel scalability for large number of processor cores. Table 5 presents the results of parallel scalability tested on the pre- and post-operative cases for large number of processor cores, including the pre-operative case with 4.04×10^6, 7.55×10^6 and 30.06×10^6

Table 7
The impact of the viscosity μ on the solver. The viscosity $\mu = 0.01$, 0.05 and 0.09 g/cm · *s* are tested for the pre- and post-operative abdominal aortas with 120 and 360 cores.

Case	Mesh	*np*	Viscosity ($g/cm \cdot s$)	Newton	GMRES	Time (*s*)	Memory (*M*)
Pre-	4.04×10^6	120	0.01	2.30	206.35	101.89	9159.83
			0.05	2.10	130.43	66.62	8416.81
			0.09	2.10	251.38	109.36	8416.81
	7.55×10^6	360	0.01	2.20	267.82	87.33	6606.50
			0.05	2.10	240.71	77.52	6323.81
			0.09	2.10	187.05	62.96	6323.81
Post-	3.99×10^6	120	0.01	2.40	195.29	99.04	8344.01
			0.05	2.10	132.19	65.30	7377.61
			0.09	2.10	94.29	31.95	5062.80
	7.35×10^6	360	0.01	2.20	339.82	98.70	5328.00
			0.05	2.10	315.71	88.82	5102.98
			0.09	2.10	175.33	55.95	5102.98

elements and the post-operative case with 3.99×10^6, 7.35×10^6 and 30.02×10^6 elements. The optimal choice of overlapping size $\delta = 8$ and subdomain solver ILU(3) is adopted. It can be seen that the memory usage drops by half when doubling the number of processor cores and the number of nonlinear iterations stays at a constant value of 2.1 for all the test cases. For the pre-operative case, we observe parallel efficiencies at 75% with 480 cores, 82% with 1440 cores and 67% with 2880 cores for the three meshes (from coarse to fine). For the post-operative case, we have 73% with 480 cores, 76% with 1440 cores and 68% with 2880 cores. To see it more clearly, the speedup versus the number of processor cores is plotted in Fig. 12. Close to linear speedup is achieved for both cases.

The impact of time-step size. Table 6 exploits the impact of time-step size Δt on the performance of the algorithm. The time-step sizes 1.00×10^{-3}, 5.00×10^{-3} and $1.00 \times 10^{-2} s$ are tested with 120 and 360 cores for the pre- and post-operative abdominal aortas. Usually, the convergence of explicit schemes is strictly restricted by the time-step size. However, our algorithm remains stable for a wide range of Δt owing to the fully implicit backward Euler method in time; meanwhile, the increasing number of Newton iterations suggests the increasing difficulty in the algebraic systems when the time-step size becomes larger. Moreover, the influence of the time-step sizes on the accuracy of the solution has been tested by the temporal variation of the pressure at $P3$, as shown in Fig. 13. A decrease of the time-step size from $\Delta t = 1.00 \times 10^{-2}$ to $\Delta t = 5.00 \times 10^{-3}$ improves the accuracy of the solution, but a further reduction to $1.00 \times 10^{-3} s$ doesn't help much.

The impact of viscosity. The viscosity is an important physical parameter of the blood flow and different patients may have different values. Table 7 shows the robust performance of the algorithm for different $\mu = 0.01$, 0.05 and 0.09 g/cm $\cdot$ s in pre- and post-operative abdominal aortas. It can be seen that the decrease of the viscosity generally leads to the increase of the compute time, the memory storage, and more importantly, the number of Newton iterations, all of which imply that the problem becomes harder to solve.

4. Concluding remarks

In this paper, a highly scalable parallel method is investigated to solve the unsteady incompressible Navier-Stokes equations for the simulation of blood flows in a full-size abdominal aorta with and without aneurysm and 12 outlets. Using the resistance boundary condition, the velocity, the pressure and the wall shear stress calculated from the pre- and post-operative abdominal aortas are compared. Results show that the aneurysm repair reduces the pressure and increases the magnitude of the velocity and the wall shear stress in the abdominal section. Temporal variations of the point-wise and the spatial-averaged wall shear stress are studied. Moreover, the parallel scalability is studied for different preconditioning parameters, including the fill-in level and the overlapping size; and the robustness of the algorithm is examined for different mesh sizes, time-step sizes and the blood viscosity. A parallel efficiency of about 70% is obtained for both pre- and post-operative cases on a parallel computer with up to 2880 processor cores. With such an approach, a patient-specific flow analysis can be obtained in about an hour using 480 processor cores, and the time can be further shortened linearly by increasing the number of processor cores. Large computing time is one of the obstacles for the applications of CFD in the surgical planning. With this highly scalable approach, we are one step closer to the goal. A statistical analysis of data from more patients will be considered in a future work.

Declaration of competing interest

The authors declare that they have no known competing financial interests or personal relationships that could have appeared to influence the work reported in this paper.

Acknowledgement

This work was partially supported by the National Key R&D Program of China (Grant No. 2018YFE0198400), the National Natural Science Foundation of China (Grant Nos. 11801543, 81871447) and the Shenzhen grant (Grant No. SZBL2019062801002).

Appendix A. Supplementary data

Supplementary data to this article can be found online at https://doi.org/10.1016/j.compbiomed.2021.104652.

References

[1] E. Akkoyun, S.T. Kwon, A.C. Acar, W. Lee, S. Baek, Predicting abdominal aortic aneurysm growth using patient-oriented growth models with two-step Bayesian inference, Comput. Biol. Med. 117 (2020) 103620.
[2] R. Antón, C.Y. Chen, M.Y. Hung, E.A. Finol, K. Pekkan, Experimental and computational investigation of the patient-specific abdominal aortic aneurysm pressure field, Comput. Methods Biomech. Biomed. Eng. 18 (2015) 981–992.
[3] A. Arzani, Accounting for residence-time in blood rheology models: do we really need non-Newtonian blood flow modelling in large arteries, J. R. Soc. Interface 15 (2018) 20180486.
[4] F. Auricchio, M. Ferretti, A. Lefieux, M. Musci, A. Reali, S. Trimarchi, A. Veneziani, Parallelizing a finite element solver in computational hemodynamics: a black box approach, Int. J. High Perform. Comput. Appl. 32 (2018) 351–362.
[5] S. Balay, S. Abhyankar, M.F. Adams, J. Brown, P. Brune, K. Buschelman, L. Dalcin, A. Dener, V. Eijkhout, W.D. Gropp, D. Karpeyev, D. Kaushik, M.G. Knepley, D. A. May, L.C. McInnes, R.T. Mills, T. Munson, K. Rupp, P. Sanan, B.F. Smith, S. Zampini, H. Zhang, H. Zhang, PETSc Users Manual, Argonne National Laboratory, 2021.
[6] A.T. Barker, X.C. Cai, Scalable parallel methods for monolithic coupling in fluid–structure interaction with application to blood flow modeling, J. Comput. Phys. 229 (2010) 642–659.
[7] L. Bertagna, S. Deparis, L. Formaggia, D. Forti, A. Veneziani, The LifeV Library: Engineering Mathematics beyond the Proof of Concept, 2017 arXiv:1710.06596 [math.NA].
[8] A.J. Boyd, D.C. Kuhn, R.J. Lozowy, G.P. Kulbisky, Low wall shear stress predominates at sites of abdominal aortic aneurysm rupture, J. Vasc. Surg. 63 (2016) 1613–1619.
[9] G.H. Chang, C.M. Schirmer, Y. Modarres-Sadeghi, A reduced-order model for wall shear stress in abdominal aortic aneurysms by proper orthogonal decomposition, J. Biomech. 54 (2017) 33–43.
[10] R. Chen, B. Wu, Z. Cheng, W.S. Shiu, J. Liu, L. Liu, Y. Wang, X. Wang, X.C. Cai, A parallel non-nested two-level domain decomposition method for simulating blood flows in cerebral artery of stroke patient, Int. J. Numer. Method Biomed. Eng. 36 (2020), e3392.
[11] P. Di Achille, G. Tellides, C. Figueroa, J. Humphrey, A haemodynamic predictor of intraluminal thrombus formation in abdominal aortic aneurysms, Proc. Math. Phys. Eng. Sci. 470 (2014) 20140163.
[12] J. Dottori, M. Casciaro, D. Craiem, S. El-Batti, E. Mousseaux, J.M. Alsac, I. Larrabide, Regional assessment of vascular morphology and hemodynamics: methodology and evaluation for abdominal aortic aneurysms after endovascular repair, Comput. Methods Biomech. Biomed. Eng. 23 (2020) 1060–1070.
[13] E.A. Finol, C.H. Amon, Blood flow in abdominal aortic aneurysms: pulsatile flow hemodynamics, J. Biomech. Eng. 123 (2001) 474–484.
[14] E.A. Finol, K. Keyhani, C.H. Amon, The effect of asymmetry in abdominal aortic aneurysms under physiologically realistic pulsatile flow conditions, J. Biomech. Eng. 125 (2003) 207–217.
[15] M. Ghaffari, K. Tangen, A. Alaraj, X. Du, F.T. Charbel, A.A. Linninger, Large-scale subject-specific cerebral arterial tree modeling using automated parametric mesh generation for blood flow simulation, Comput. Biol. Med. 91 (2017) 353–365.
[16] Q. Ghulam, K. Bredahl, L. Lönn, L. Rouet, H. Sillesen, J. Eiberg, Follow-up on small abdominal aortic aneurysms using three dimensional ultrasound: volume versus diameter, Eur. J. Vasc. Endovasc. Surg. 54 (2017) 439e445.
[17] D. Groen, J. Hetherington, H.B. Carver, R.W. Nash, M.O. Bernabeu, P.V. Coveney, Analysing and modelling the performance of the HemeLB lattice-Boltzmann simulation environment, J. Comput. Sci. 4 (2013) 412–422.
[18] D. Hardman, S.I. Semple, J.M. Richards, P.R. Hoskins, Comparison of patient-specific inlet boundary conditions in the numerical modelling of blood flow in abdominal aortic aneurysm disease, Int. J. Numer. Meth. Bio. 29 (2013) 165–178.
[19] H. Jalalzadeh, R. Indrakusuma, R. Planken, D. Legemate, M. Koelemay, R. Balm, Inflammation as a predictor of abdominal aortic aneurysm growth and rupture: a systematic review of imaging biomarkers, Eur. J. Vasc. Endovasc. Surg. 52 (2016) 333–342.
[20] Z. Jiang, H.N. Do, J. Choi, W. Lee, S. Baek, A deep learning approach to predict abdominal aortic aneurysm expansion using longitudinal data, Front. Physiol. 7 (2020) 235.
[21] F. Joly, G. Soulez, D. Garcia, S. Lessard, C. Kauffmann, Flow stagnation volume and abdominal aortic aneurysm growth: insights from patient-specific computational flow dynamics of Lagrangian-coherent structures, Comput. Biol. Med. 92 (2018) 98–109.

[22] G. Karypis, K. Schloegel, V. Kumar, ParMETIS: Parallel Graph Partitioning and Sparse Matrix Ordering Library, Department of Computer Science and Engineering, University of Minnesota, 2013.
[23] K.C. Kent, Abdominal aortic aneurysms, N. Engl. J. Med. 371 (2014) 2101–2108.
[24] R. Khlebnikov, C.A. Figueroa, Crimson: towards a Software Environment for Patient-specific Blood Flow Simulation for Diagnosis and Treatment, Workshop on Clinical Image-Based Procedures, 2015, pp. 10–18.
[25] F. Kong, V. Kheyfets, E. Finol, X.C. Cai, An efficient parallel simulation of unsteady blood flows in patient-specific pulmonary artery, Int. J. Numer. Method Biomed. Eng. 34 (2018), e2952.
[26] F. Kong, V. Kheyfets, E. Finol, X.C. Cai, Simulation of unsteady blood flows in a patient-specific compliant pulmonary artery with a highly parallel monolithically coupled fluid-structure interaction algorithm, Int. J. Numer. Method Biomed. Eng. 35 (2019), e3208.
[27] D. Kumar, R. Vinoth, R. Adhikari, V. Shankar, Non-Newtonian and Newtonian blood flow in human aorta: a transient analysis, Biomed. Res. 28 (2017), 3194–3194.
[28] H. Lan, A. Updegrove, N.M. Wilson, G.D. Maher, S.C. Shadden, A.L. Marsden, A re-engineered software interface and workflow for the open source SimVascular cardiovascular modeling package, J. Biomech. Eng. 140 (2018), 024501.
[29] J. Lantz, J. Renner, M. Karlsson, Wall shear stress in a subject specific human aorta–influence of fluid-structure interaction, Int. J. Appl. Mech. 3 (2011) 759–778.
[30] A.S. Les, S.C. Shadden, C.A. Figueroa, J.M. Park, M.M. Tedesco, R.J. Herfkens, R. L. Dalman, C.A. Taylor, Quantification of hemodynamics in abdominal aortic aneurysms during rest and exercise using magnetic resonance imaging and computational fluid dynamics, Ann. Biomed. Eng. 38 (2010) 1288–1313.
[31] W. Li, L. Luo, Finite volume lattice Boltzmann method for nearly incompressible flows on arbitrary unstructured meshes, Commun. Comput. Phys. 20 (2016) 301–324.
[32] M.L. Liljeqvist, R. Hultgren, T.C. Gasser, J. Roy, Volume growth of abdominal aortic aneurysms correlates with baseline volume and increasing finite element analysis-derived rupture risk, J. Vasc. Surg. 63 (2016) 1434–1442.
[33] M.D. Mazzeo, P.V. Coveney, HemeLB: a high performance parallel lattice-Boltzmann code for large scale fluid flow in complex geometries, Comput. Phys. Commun. 178 (2008) 894–914.
[34] O. Meyrignac, L. Bal, C. Zadro, A. Vavasseur, A. Sewonu, M. Gaudry, B. Saint-Lebes, M. De Masi, P. Revel-Mouroz, A. Sommet, et al., Combining volumetric and wall shear stress analysis from ct to assess risk of abdominal aortic aneurysm progression, Radiology 295 (2020) 722–729.
[35] P.D. Morris, A. Narracott, H. von Tengg-Kobligk, D.A.S. Soto, S. Hsiao, A. Lungu, P. Evans, N.W. Bressloff, P.V. Lawford, D.R. Hose, et al., Computational fluid dynamics modelling in cardiovascular medicine, Heart 102 (2016) 18–28.
[36] K. Novak, S. Polzer, T. Krivka, R. Vlachovsky, R. Staffa, L. Kubicek, L. Lambert, J. Bursa, Correlation between transversal and orthogonal maximal diameters of abdominal aortic aneurysms and alternative rupture risk predictors, Comput. Biol. Med. 83 (2017) 151–156.
[37] B. Owen, C. Lowe, N. Ashton, P. Mandal, S. Rogers, W. Wein, C. McCollum, A. Revell, Computational hemodynamics of abdominal aortic aneurysms: three-dimensional ultrasound versus computed tomography, J. Eng. Med. 230 (2016) 201–210.
[38] G.E. Pieles, G. Szantho, J.C. Rodrigues, C.B. Lawton, A.G. Stuart, C. Bucciarelli-Ducci, M.S. Turner, C.A. Williams, R.M. Tulloh, M.C. Hamilton, Adaptations of aortic and pulmonary artery flow parameters measured by phase-contrast magnetic resonance angiography during supine aerobic exercise, Eur. J. Appl. Physiol. 114 (2014) 1013–1023.
[39] A. Polanczyk, A. Piechota, CFD simulations of blood flow through abdominal part of aorta, Chall. Mod. Technol. 1 (2010) 34–39.
[40] S. Polzer, T.C. Gasser, R. Vlachovský, L. Kubíček, L. Lambert, V. Man, K. Novák, M. Slažanský, J. Burša, R. Staffa, Biomechanical indices are more sensitive than diameter in predicting rupture of asymptomatic abdominal aortic aneurysms, J. Vasc. Surg. 71 (2020) 617–626.
[41] Y. Qiu, D. Yuan, Y. Wang, J. Wen, T. Zheng, Hemodynamic investigation of a patient-specific abdominal aortic aneurysm with iliac artery tortuosity, Comput. Methods Biomech. Biomed. Eng. 21 (2018) 824–833.
[42] B. Rengarajan, W. Wu, C. Wiedner, D. Ko, S.C. Muluk, M.K. Eskandari, P.G. Menon, E.A. Finol, A comparative classification analysis of abdominal aortic aneurysms by machine learning algorithms, Ann. Biomed. Eng. 48 (2020) 1419–1429.
[43] P. Reymond, F. Merenda, F. Perren, D. Rüfenacht, N. Stergiopulos, Validation of a one-dimensional model of the systemic arterial tree, Am. J. Physiol-Heart C 297 (2009) 208–222.
[44] Z. Sun, T. Chaichana, Y.B. Allen, M. Sangworasil, S. Tungjitkusolmun, D.E. Hartley, M.M. Lawrence-Brown, Investigation of hemodynamic changes in abdominal aortic aneurysms treated with fenestrated endovascular grafts, in: 13th Int. Conf. Biomed. Eng., Springer, 2009, pp. 1676–1679.
[45] Z.H. Sun, Abdominal aortic aneurysm: treatment options, image visualizations and follow-up procedures, J. Geriatr. Cardiol. 9 (2012) 49.
[46] K.M. Tse, P. Chiu, H.P. Lee, P. Ho, Investigation of hemodynamics in the development of dissecting aneurysm within patient-specific dissecting aneurismal aortas using computational fluid dynamics (CFD) simulations, J. Biomech. 44 (2011) 827–836.
[47] A. Updegrove, N.M. Wilson, J. Merkow, H. Lan, A.L. Marsden, S.C. Shadden, SimVascular: an open source pipeline for cardiovascular simulation, Ann. Biomed. Eng. 45 (2017) 525–541.
[48] C. Vergara, D. Le Van, M. Quadrio, L. Formaggia, M. Domanin, Large eddy simulations of blood dynamics in abdominal aortic aneurysms, Med. Eng. Phys. 47 (2017) 38–46.
[49] I.E. Vignon-Clementel, C.A. Figueroa, K.E. Jansen, C.A. Taylor, Outflow boundary conditions for three-dimensional finite element modeling of blood flow and pressure in arteries, Comput. Methods Appl. Math. 195 (2006) 3776–3796.
[50] R. Vinoth, D. Kumar, R. Adhikari, S. Vijayapradeep, K. Geetha, R. Ilavarasi, S. Mahalingam, Steady and transient flow CFD simulations in an aorta model of normal and aortic aneurysm subjects, in: Int. Conf. Sens. Imaging, Springer, 2017, pp. 29–43.
[51] Y. Wu, X.C. Cai, A parallel two-level method for simulating blood flows in branching arteries with the resistive boundary condition, Comput. Fluids 45 (2011) 92–102.
[52] Y. Wu, X.C. Cai, A fully implicit domain decomposition based ale framework for three-dimensional fluid–structure interaction with application in blood flow computation, J. Comput. Phys. 258 (2014) 524–537.
[53] P. Youssefi, A. Gomez, C. Arthurs, R. Sharma, M. Jahangiri, C.A. Figueroa, Impact of patient-specific inflow velocity profile on hemodynamics of the thoracic aorta, J. Biomech. Eng. 140 (2018), 011002.
[54] B.A. Zambrano, H. Gharahi, C. Lim, F.A. Jaberi, J. Choi, W. Lee, S. Baek, Association of intraluminal thrombus, hemodynamic forces, and abdominal aortic aneurysm expansion using longitudinal CT images, Ann. Biomed. Eng. 44 (2016) 1502–1514.
[55] M. Zhou, Petascale Adaptive Computational Fluid Dynamics, Ph.D. thesis, Rensselaer Polytechnic Institute, 2009.
[56] M. Zhou, O. Sahni, H.J. Kim, C.A. Figueroa, C.A. Taylor, M.S. Shephard, K. E. Jansen, Cardiovascular flow simulation at extreme scale, Comput. Mech. 46 (2010) 71–82.
[57] M. Ziegler, M. Welander, J. Lantz, M. Lindenberger, N. Bjarnegård, M. Karlsson, T. Ebbers, T. Länne, P. Dyverfeldt, Visualizing and quantifying flow stasis in abdominal aortic aneurysms in men using 4D flow MRI, Magn. Reson. Imaging 57 (2019) 103–110.